This article was downloaded by: *[University of Illinois]*
On: *29 September 2008*
Access details: *Access Details: [subscription number 790943743]*
Publisher *Taylor & Francis*
Informa Ltd Registered in England and Wales Registered Number: 1072954 Registered office: Mortimer House, 37-41 Mortimer Street, London W1T 3JH, UK

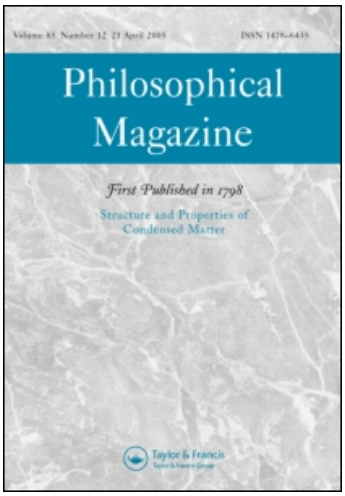


**Philosophical Magazine**
Publication details, including instructions for authors and subscription information:
http://www.informaworld.com/smpp/title~content=t713695589

# Boundary condition effects on multiscale analysis of damage localization

Helen M. Inglis [a]; Philippe H. Geubelle [b]; Karel Matouš [bc]
[a] Department of Mechanical Science and Engineering, University of Illinois at Urbana-Champaign, Urbana, IL 61801, USA [b] Department of Aerospace Engineering, University of Illinois at Urbana-Champaign, Urbana, IL 61801, USA [c] Computational Science and Engineering, University of Illinois at Urbana-Champaign, Urbana, IL 61801, USA

Online Publication Date: 01 June 2008

**To cite this Article** Inglis, Helen M., Geubelle, Philippe H. and Matouš, Karel(2008)'Boundary condition effects on multiscale analysis of damage localization',Philosophical Magazine,88:16,2373 — 2397
**To link to this Article: DOI:** 10.1080/14786430802345645
**URL:** http://dx.doi.org/10.1080/14786430802345645

PLEASE SCROLL DOWN FOR ARTICLE

Full terms and conditions of use: http://www.informaworld.com/terms-and-conditions-of-access.pdf

This article may be used for research, teaching and private study purposes. Any substantial or systematic reproduction, re-distribution, re-selling, loan or sub-licensing, systematic supply or distribution in any form to anyone is expressly forbidden.

The publisher does not give any warranty express or implied or make any representation that the contents will be complete or accurate or up to date. The accuracy of any instructions, formulae and drug doses should be independently verified with primary sources. The publisher shall not be liable for any loss, actions, claims, proceedings, demand or costs or damages whatsoever or howsoever caused arising directly or indirectly in connection with or arising out of the use of this material.

*Philosophical Magazine*
Vol. 88, No. 16, 1 June 2008, 2373–2397

Taylor & Francis
Taylor & Francis Group

# Boundary condition effects on multiscale analysis of damage localization

Helen M. Inglis[a]*, Philippe H. Geubelle[b] and Karel Matouš[bc]

[a]*Department of Mechanical Science and Engineering, University of Illinois at Urbana-Champaign, 1206 W Green St, Urbana, IL 61801, USA;* [b]*Department of Aerospace Engineering, University of Illinois at Urbana-Champaign, 104 S. Wright St, Urbana, IL 61801, USA;* [c]*Computational Science and Engineering, University of Illinois at Urbana-Champaign, 1304 W. Springfield Ave, Urbana, IL 61801, USA*

(*Received 29 October 2007; final version received 14 May 2008*)

Downloaded By: [University of Illinois] At: 17:27 29 September 2008

The choice of boundary conditions used in multiscale analysis of heterogeneous materials affects the numerical results, including the macroscopic constitutive response, the type and extent of damage taking place at the microscale and the required size of the Representative Volume Element (RVE). We compare the performance of periodic boundary conditions and minimal kinematic boundary conditions applied to the unit cell of a particulate composite material, both in the absence and presence of damage at the particle–matrix interfaces. In particular, we investigate the response of the RVE under inherently non-periodic loading conditions, and the ability of both boundary conditions to capture localization events that are not aligned with the RVE boundaries. We observe that, although there are some variations in the evolution of the microscale damage between the two methods, there is no significant difference in homogenized responses even when localization is not aligned with the cell boundaries.

**Keywords:** multiscale analysis; cohesive damage; periodic boundary conditions; representative volume element; localization

## 1. Introduction

In multiscale numerical schemes, microscale simulations are performed on a base cell that represents the microstructure but is small enough to be computationally tractable. This Representative Volume Element (RVE) may be as simple as a cell containing a single particle for an ordered microstructure, but is usually larger and more complex. Theoretically, the RVE must be sufficiently large to include all the physical processes taking place at the microstructural level, and sufficiently small to be idealized as a material point at the macroscale [1]. Determining the size at which a volume element is representative has been the topic of much study. Among the many tools employed to investigate the geometric statistics of the RVE are the pair distribution function introduced by Pyrz [2] and the two-point probability function used by Zeman and Šejnoha [3] and by Kumar et al. [4]. Considering mechanical properties, Kanit et al. [1] have shown that the required RVE size depends on the choice of boundary conditions.

*Corresponding author. Email: hinglis@uiuc.edu

ISSN 1478–6435 print/ISSN 1478–6443 online
© 2008 Taylor & Francis
DOI: 10.1080/14786430802345645
http://www.informaworld.com

Additionally, Swaminathan and Ghosh [5] have shown that RVE size is dependent on the presence of damage in the microstructure.

A key aspect of RVE-based multiscale modelling is the boundary conditions used to capture the effect of the surrounding medium. The true traction or displacement fields at the boundary of an RVE in a surrounding microstructure cannot be evaluated without solving the larger problem, which is prohibitively expensive. One must therefore make simplifying assumptions about the way in which load is transferred between a cell in a heterogeneous microstructure and the surrounding material. Since the cell is sufficiently small to be considered a material point at the macroscale, it is reasonable to assume that it should experience macroscopically uniform stress and strain fields. The simplest way to impose this condition at the microscale is as a uniform traction field or a linear displacement field on the cell boundaries. It is immediately apparent that such boundary conditions will not be accurate, since we do not expect straight lines in an undeformed heterogeneous microstructure to remain straight under deformation. Linear displacement and uniform traction boundary conditions provide an upper bound (Voigt bound) and lower bound (Reuss bound) for the solution, respectively.

Another approach to account for interactions between the RVE and surrounding microstructure is based on the assumption that the RVE is periodic, representing one cell in an infinite array of repeating cells. Under the action of a macroscopic strain applied to every point of the microscale domain, the cell is free to deform in any manner, subject only to the constraint that homologous points on opposite boundaries experience the same fluctuating displacements and opposite tractions. Periodic boundary conditions are widely used in multiscale analysis, see for example the work by Guedes and Kikuchi [6], Ghosh et al. [7], Fish et al. [8] and Matouš and Geubelle [9]. They offer some benefits over other boundary conditions, the most significant advantage being the extensive mathematical and theoretical framework that supports them [10–12]. Periodic boundary conditions naturally simulate the constraining effect of the surrounding material, although that constraint is in error when the microstructure is other than periodic.

Kanit et al. [1] compare uniform traction and linear displacement boundary conditions with periodic boundary conditions for undamaged particulate composites. They study the convergence results for increasing RVE size, averaged over a number of different realizations of the random microstructure, and show that the stiffness response for an RVE under periodic boundary conditions falls between the bounds provided by the two other boundary conditions. They note, however, that the error bars on periodic boundary conditions are higher than for the other two boundary conditions. In a comparison with mixed boundary conditions, van der Sluis et al. [13] observe that periodic boundary conditions are more appropriate for modelling periodic or nearly periodic structures.

Mesarovic and Padbidri [14] contend that periodic boundary conditions impose unphysical constraints on the unit cell. Under loading conditions which are not inherently periodic, such as shear loading, periodic boundary conditions result in a stiffer constitutive response and inhibit localization that is not aligned with the cell boundaries. They propose the use of *Minimal Kinematic Boundary Conditions* (MKBC), in which the macroscopic loading is satisfied in a weak sense through a boundary integral, rather than at every point in the material domain. They demonstrate results for an undamaged polycrystal, showing slightly faster convergence of the shear modulus RVE size for minimal kinematic as opposed to Periodic Boundary Conditions (PBC). Fast Fourier transforms of the PBC

Downloaded By: [University of Illinois] At: 17:27 29 September 2008

shear stress fields show a spurious wavelength due to the unit cell size, which disappears under MKBC. They argue that localization behaviour will be improved by using MKBC.

Prompted by the results of Mesarovic and Padbidri, we investigate in this paper the effect of boundary conditions on the response of a 50% volume fraction particulate composite system with linear elastic constituents. We start by revisiting their comparison of shear stiffness calculated under PBC and MKBC for an undamaged material. We then extend their study to consider localization behaviour in a composite system with damage to the particle–matrix interface. We compare the effectiveness of each boundary condition in capturing the macroscopic and microstructural behaviour of the RVE. We present figures which compare the deformed shape of the RVE under each boundary condition for both uniaxial strain and shear loading. We aim to determine which boundary conditions should be used in modelling microstructures that might experience localization. The numerical results are built on an analytical comparison between the two results enabled by expressing MKBC in the same asymptotic framework as PBC. It should be emphasized that since only particle–matrix debonding is considered in this work, only weak or partial localization is observed. To observe true localization, matrix tearing would also need to be modelled. However, once complete localization has occurred, the RVE will no longer be statistically homogeneous, and multiscale analysis will require the transfer of additional gradient-based measures to the macroscale [15,16].

Failure of the interface between inclusions and binder is modelled using a bilinear cohesive law. We use linear kinematics and linear elastic material models, and admit only the nonlinearity due to the cohesive failure of the particle–matrix interface. The material properties chosen include a large stiffness mismatch between the inclusions and the compressible matrix. The comparison is performed in two dimensions using a plane strain assumption, under which the circular inclusions represent fibers rather than particles, although we often refer to the inclusions as particles. We also refer to the base cell used in multiscale computations as an RVE without actually proving that it is representative, as the determination of the representativity of the unit cell is not the focus of this study. The primary objective of the present work is instead to compare the multiscale predictions associated with the two boundary conditions on the same unit cells with and without damage.

The mathematical formulation of the multiscale scheme associated with the two boundary conditions is presented in Section 2, and the numerical implementation follows in Section 3. The two boundary conditions are then compared under shear loading in Section 4 and under uniaxial loading in Section 5.

## 2. Multiscale formulation

Consider the system shown in Figure 1, a macroscale body $\Omega$ consisting of a matrix containing particles which are very small by comparison with the body. The deformation of a material point, $\boldsymbol{x} \in \Omega$, depends not only on the traction and displacement boundary conditions imposed on the boundary $\Gamma = \Gamma_t \cup \Gamma_d$, but also on the microstructure in the immediate neighbourhood of $\boldsymbol{x}$, which we denote by $\Theta$. $\Theta$ is assumed to be $\boldsymbol{y}$-periodic, and from our vantage point at the microscale, this is a reasonably good assumption. Particles are permitted to debond from the matrix, with cohesive tractions $\boldsymbol{T}$ at the particle–matrix interface $\Gamma_c$ given by a traction-separation law, which is described in Section 3.1. Note that

Downloaded By: [University of Illinois] At: 17:27 29 September 2008

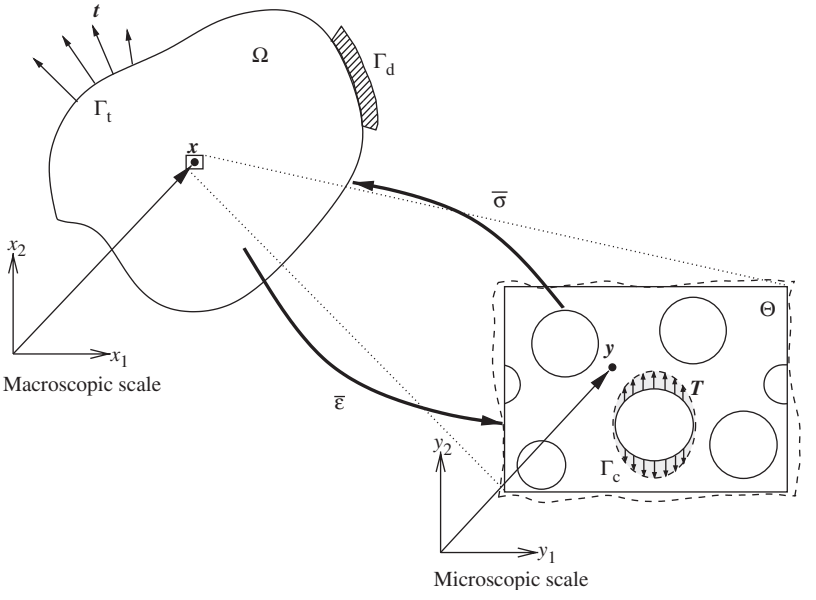


Figure 1. Schematic representation of the multiscale problem with $\bar{\boldsymbol{\sigma}}$ and $\bar{\boldsymbol{\varepsilon}}$ denoting the macroscopic stress and strain fields, respectively. Heterogeneities and discontinuities are visible only at the microscale. $\boldsymbol{T}$ represents the cohesive traction vector acting along the particle–matrix interface $\Gamma_c$.

the heterogeneities and discontinuities present at the microscale are not visible at the macroscale, where the analysis is performed on the homogenized medium.

Bold quantities represent vectors, tensors or matrices. Lower-case Roman letters (e.g. $\boldsymbol{u}$) indicate vectors, lower-case Greek letters (e.g. $\boldsymbol{\sigma}$) denote second-order tensors, and upper-case Roman letters (e.g. $\boldsymbol{K}$) denote either higher-order tensors or matrices. Indicial notation is used, with indices taking values of 1, 2 and 3, and summation implied. Although the numerical analysis is performed in 2D, the mathematical formulation is presented in a fully 3D setting.

### 2.1. *Periodic boundary conditions*

Microscale points $\boldsymbol{y} \in \Theta$ are related to points at the macroscale through $\boldsymbol{y} = \boldsymbol{x}/\xi$, where $\xi$ is an asymptotic scaling parameter, $|\xi| \ll 1$. Domain $\Theta$ is assumed to be $\boldsymbol{y}$-periodic.

The displacement field, $\boldsymbol{u} = \boldsymbol{u}(\boldsymbol{x}, \boldsymbol{y})$, which has both macro-and microscale dependence, can be expanded asymptotically [12] as

$$\boldsymbol{u}(\boldsymbol{x}, \boldsymbol{y}) \approx \boldsymbol{u}^{(0)}(\boldsymbol{x}, \boldsymbol{y}) + \xi^1 \boldsymbol{u}^{(1)}(\boldsymbol{x}, \boldsymbol{y}) + \xi^2 \boldsymbol{u}^{(2)}(\boldsymbol{x}, \boldsymbol{y}) + \cdots, \tag{1}$$

where superscripts in parentheses represent the asymptotic order of the terms. Applying the differentiation operator

$$\frac{\partial \phi(\boldsymbol{x}, \boldsymbol{y})}{\partial \boldsymbol{x}} = \frac{\partial \phi}{\partial \boldsymbol{x}} + \frac{1}{\xi} \frac{\partial \phi}{\partial \boldsymbol{y}}, \tag{2}$$

Downloaded By: [University of Illinois] At: 17:27 29 September 2008

we find the asymptotic expansion of the strain,

$$\varepsilon_{ij} \approx \xi^{-1}\varepsilon_{ij}^{(-1)} + \xi^{0}\varepsilon_{ij}^{(0)} + \xi^{1}\varepsilon_{ij}^{(1)} + \cdots. \tag{3}$$

Introducing the symmetric gradient operator

$$\frac{\partial^S \bullet_i}{\partial x_j} = \frac{1}{2}\left(\frac{\partial \bullet_i}{\partial x_j} + \frac{\partial \bullet_j}{\partial x_i}\right), \tag{4}$$

it can easily be verified that

$$\varepsilon_{ij}^{(-1)} = \frac{\partial^S u_i^{(0)}}{\partial y_j}, \quad \varepsilon_{ij}^{(0)} = \frac{\partial^S u_i^{(0)}}{\partial x_j} + \frac{\partial^S u_i^{(1)}}{\partial y_j}, \quad \varepsilon_{ij}^{(1)} = \frac{\partial^S u_i^{(1)}}{\partial x_j} + \frac{\partial^S u_i^{(2)}}{\partial y_j}. \tag{5}$$

The Principle of Virtual Work for this system is given by

$$\int_\Omega C_{ijkl}\varepsilon_{kl}\frac{\partial^S v_i}{\partial x_j}\mathrm{d}\Omega - \int_{\Gamma_t} t_i v_i \,\mathrm{d}S + \int_{\Gamma_c} T_i \lfloor v_i \rceil \mathrm{d}S = 0, \tag{6}$$

where $\boldsymbol{C}(\boldsymbol{x}, \boldsymbol{y})$ is the material stiffness tensor, $\boldsymbol{t}$ are the external tractions applied on $\Gamma_t$ and $\boldsymbol{v}$ is any admissible virtual displacement. The notation $\lfloor \bullet \rceil$ indicates the discontinuity in the field $\bullet$. Note that $\boldsymbol{u}$ is assumed to be continuous in $\boldsymbol{x}$, with all discontinuities occurring only at the microscale. Substituting (1) and (3) into (6), expanding and grouping by powers of $\xi$, we find

$$\frac{1}{\xi^2}\int_\Omega C_{ijkl}\frac{\partial^S u_k^{(0)}}{\partial y_l}\frac{\partial^S v_i}{\partial y_j}\,\mathrm{d}\Omega = 0, \tag{7}$$

$$\frac{1}{\xi}\int_\Omega C_{ijkl}\left[\left(\frac{\partial^S u_k^{(0)}}{\partial x_l} + \frac{\partial^S u_k^{(1)}}{\partial y_l}\right)\frac{\partial^S v_i}{\partial y_j} + \frac{\partial^S u_k^{(0)}}{\partial y_l}\frac{\partial^S v_i}{\partial x_j}\right]\mathrm{d}\Omega + \int_{\Gamma_c} T_i \lfloor v_i \rceil \mathrm{d}S = 0, \tag{8}$$

$$\int_\Omega C_{ijkl}\left[\left(\frac{\partial^S u_k^{(1)}}{\partial x_l} + \frac{\partial^S u_k^{(2)}}{\partial y_l}\right)\frac{\partial^S v_i}{\partial y_j} + \left(\frac{\partial^S u_k^{(0)}}{\partial x_l} + \frac{\partial^S u_k^{(1)}}{\partial y_l}\right)\frac{\partial^S v_i}{\partial x_j}\right]\mathrm{d}\Omega = \int_{\Gamma_t} t_i v_i \,\mathrm{d}S. \tag{9}$$

The development of these terms is presented in considerable detail by Guedes and Kikuchi [6], and only the pertinent results are described here.

We make use of the first of the integration operators for $\boldsymbol{y}$-periodic functions

$$\begin{aligned} \lim_{\xi\to 0^+}\int_\Omega \phi\left(\frac{\boldsymbol{x}}{\xi}\right)\mathrm{d}\Omega &= \frac{1}{|\Theta|}\int_\Omega\int_\Theta \phi(\boldsymbol{y})\mathrm{d}\Theta\,\mathrm{d}\Omega \\ \lim_{\xi\to 0^+}\xi\int_{\partial\Omega} \phi\left(\frac{\boldsymbol{x}}{\xi}\right)\mathrm{d}S &= \frac{1}{|\Theta|}\int_\Omega\int_{\partial\Theta} \phi(\boldsymbol{y})\mathrm{d}S\,\mathrm{d}\Omega \end{aligned} \tag{10}$$

and the arbitrariness of $\boldsymbol{v}$ to reduce (7) for one macroscopic point to

$$\int_\Theta C_{ijkl}\frac{\partial^S u_k^{(0)}}{\partial y_l}\frac{\partial^S v_i}{\partial y_j}\mathrm{d}\Theta = 0 \tag{11}$$

Downloaded By: [University of Illinois] At: 17:27 29 September 2008

and then integrate by parts, resulting in

$$\int_{\partial\Theta} C_{ijkl}\frac{\partial^S u_k^{(0)}}{\partial y_l} v_i n_j \,\mathrm{d}S - \int_{\Theta} \frac{\partial}{\partial y_j}\left(C_{ijkl}\frac{\partial^S u_k^{(0)}}{\partial y_l}\right) v_i \,\mathrm{d}\Theta = 0. \tag{12}$$

The boundary term in (12) vanishes due to $\boldsymbol{y}$-periodicity of $\boldsymbol{C}$, $\boldsymbol{u}^{(0)}$ and $\boldsymbol{v}$. Arbitrariness of $\boldsymbol{v}$ requires

$$\frac{\partial}{\partial y_j}\left(C_{ijkl}\frac{\partial^S u_k^{(0)}}{\partial y_l}\right) = \boldsymbol{0}, \tag{13}$$

hence the first-order displacement term $\boldsymbol{u}^{(0)}$ is permitted to have neither microscale dependence nor discontinuities:

$$\boldsymbol{u}^{(0)}(\boldsymbol{x},\boldsymbol{y}) = \boldsymbol{u}^{(0)}(\boldsymbol{x}). \tag{14}$$

We refer to $\boldsymbol{u}^{(0)}$ as the *macroscopic displacement*. The above relation allows us to simplify (8), resulting in an expression of equilibrium at the microscale:

$$\frac{1}{|\Theta|}\int_{\Theta} C_{ijkl}\left[\left(\frac{\partial^S u_k^{(0)}(\boldsymbol{x})}{\partial x_l} + \frac{\partial^S u_k^{(1)}}{\partial y_l}\right)\frac{\partial^S v_i}{\partial y_j}\right]\mathrm{d}\Theta + \frac{1}{|\Theta|}\int_{\Gamma_c} T_i \lfloor v_i \rceil \mathrm{d}S = 0, \tag{15}$$

where admissible virtual displacements $\boldsymbol{v}(\boldsymbol{y})$ must be $\boldsymbol{y}$-periodic. Recalling (5), we note that the zero-order strain term $\boldsymbol{\varepsilon}^{(0)}$ contained in (15) consists of the macroscale gradient of the macroscopic displacement, and the microscale gradient of the first order displacement term, $\boldsymbol{u}^{(1)}$, referred to in this paper as the *fluctuating displacement*. This motivates us to rewrite the strain $\boldsymbol{\varepsilon}^{(0)}$ into macroscopic ($\bar{\boldsymbol{\varepsilon}}$) and fluctuating ($\tilde{\boldsymbol{\varepsilon}}$) components as

$$\boldsymbol{\varepsilon}^{(0)}(\boldsymbol{x},\boldsymbol{y}) = \bar{\boldsymbol{\varepsilon}}(\boldsymbol{x}) + \tilde{\boldsymbol{\varepsilon}}(\boldsymbol{x},\boldsymbol{y}), \tag{16}$$

where

$$\bar{\boldsymbol{\varepsilon}} = \frac{\partial^S \boldsymbol{u}^{(0)}}{\partial \boldsymbol{x}}, \quad \tilde{\boldsymbol{\varepsilon}} = \frac{\partial^S \boldsymbol{u}^{(1)}}{\partial \boldsymbol{y}}. \tag{17}$$

Rearranging (15), we find the following relation for the fluctuating displacement $\boldsymbol{u}^{(1)}$:

$$\frac{1}{|\Theta|}\int_{\Theta} C_{ijkl}\,\tilde{\varepsilon}_{kl}\frac{\partial^S v_i(\boldsymbol{y})}{\partial y_j}\mathrm{d}\Theta + \frac{1}{|\Theta|}\int_{\Gamma_c} T_i \lfloor v_i \rceil \,\mathrm{d}S = -\frac{1}{|\Theta|}\int_{\Theta} C_{ijkl}\,\bar{\varepsilon}_{kl}\frac{\partial^S v_i(\boldsymbol{y})}{\partial y_j}\mathrm{d}\Theta, \tag{18}$$

where the macroscopic strain $\bar{\boldsymbol{\varepsilon}}$ appears as a forcing term at the microscale.

Equation (9), the expression of equilibrium at the macroscale, is trivially satisfied in this work as we solve the microscale problem under the action of a prescribed macroscopic strain history, but do not solve the fully coupled multiscale problem.

### 2.2. *Minimal kinematic boundary conditions*

As discussed in Section 1, Mesarovic and Padbidri [14] identify unnecessary additional constraints when periodic boundary conditions are used to model shear loading.

Downloaded By: [University of Illinois] At: 17:27 29 September 2008

Their proposed minimal kinematic boundary conditions impose no constraint on the deformed shape of the body other than that it satisfy the imposed macroscopic strain.

They begin by adopting the definition of the imposed macroscopic strain $\boldsymbol{E}$ proposed by Bishop and Hill [16]:

$$E_{ij} = \frac{1}{|\Theta|}\int_{\Theta} \varepsilon_{ij}\,\mathrm{d}\Theta. \tag{19}$$

In the case of a domain containing voids, this definition is extended [17], giving

$$E_{ij} = \frac{1}{|\Theta|}\int_{\Theta_{\text{solid}}} \varepsilon_{ij}\mathrm{d}\Theta + \frac{1}{2|\Theta|}\int_{\Gamma_c} (u_i n_j + u_j n_i)\mathrm{d}S, \tag{20}$$

where the domain is partitioned into solid and void regions with $\Theta = \Theta_{\text{solid}} \cup \Theta_{\text{void}}$. The surface of the voids is given by $\Gamma_c = \partial\Theta_{\text{void}}$ with outward normal $\boldsymbol{n}$. Using the strain-displacement relation and the divergence theorem on the first term of (20), and noting that the contributions from the voids cancel out, we find

$$E_{ij} = \frac{1}{2|\Theta|}\int_{\partial\Theta} \big(u_i n_j + u_j n_i\big)\mathrm{d}S\,, \tag{21}$$

where $\boldsymbol{n}$ is the unit outward normal of $\partial\Theta$, the outer boundary of $\Theta$. Thus one can impose the macroscopic strain $\boldsymbol{E}$ by imposing the integral boundary conditions (21), provided that rigid body motion be eliminated through requiring selected points to remain fixed. Uniqueness of the solution has been proved for nonporous media by Mesarovic and Padbidri [1] and for porous media by Gurson [18].

The minimal kinematic boundary conditions can be recast within the MTH framework, beginning by assuming a first order asymptotic expansion of the displacement field,

$$\boldsymbol{u}(\boldsymbol{x},\boldsymbol{y}) \approx \boldsymbol{u}^{(0)}(\boldsymbol{x},\boldsymbol{y}) + \xi^1 \boldsymbol{u}^{(1)}(\boldsymbol{x},\boldsymbol{y}). \tag{22}$$

Note that, in contrast to the development in Section 2.1, no assumption of microscale periodicity is made in this formulation. This results in a similar system of three scale-separated equilibrium equations as (7)–(9). Based on (21), the admissible virtual displacement field under MKBC must satisfy

$$\int_{\partial\Theta} \big(v_i n_j + v_j n_i\big)\mathrm{d}S = 0. \tag{23}$$

The first scale separated Equation (7) leads again to (12), which can be rewritten

$$\frac{1}{2}\int_{\partial\Theta} (v_i n_j + v_j n_i)\, C_{ijkl}\frac{\partial^S u_k^{(0)}}{\partial y_l}\mathrm{d}S - \int_{\Theta} v_i \frac{\partial}{\partial y_j}\left(C_{ijkl}\frac{\partial^S u_k^{(0)}}{\partial y_l}\right)\mathrm{d}\Theta = 0. \tag{24}$$

Noting (23), (24) is satisfied when

$$C_{ijkl}\frac{\partial^S u_k^{(0)}}{\partial y_l} = \text{constant in } \boldsymbol{y} \;\Rightarrow\; \boldsymbol{u}^{(0)}(\boldsymbol{x},\boldsymbol{y}) = \boldsymbol{u}^{(0)}(\boldsymbol{x}) \tag{25}$$

Downloaded By: [University of Illinois] At: 17:27 29 September 2008

exactly as we have previously shown in the case of periodic boundary conditions. Here $\boldsymbol{u}^{(0)}$ can be identified with $\boldsymbol{Ex}$, and (22) becomes

$$\boldsymbol{u}(\boldsymbol{x},\boldsymbol{y}) \approx \boldsymbol{Ex} + \xi^1 \boldsymbol{u}^{(1)}(\boldsymbol{x},\boldsymbol{y}). \tag{26}$$

We see that the definitions of $\boldsymbol{E}$ and $\bar{\boldsymbol{\varepsilon}}$ coincide, facilitating comparison between the two boundary conditions. Miehe [18] shows that constant stress boundary conditions, linear displacement boundary conditions and periodic boundary conditions all satisfy the constraints required of a fluctuating displacement field in a homogenization problem. It is clear that minimal kinematic boundary conditions are an additional class of boundary conditions which satisfy these constraints by construction. We shall compare fluctuating displacement fields obtained under each boundary condition in Section 3.4.

## 3. Finite element implementation

The problem is solved using a standard cohesive finite element formulation. The material models are linear elastic, with particles much stiffer than the matrix. The simulations are performed using linear kinematics, in a two-dimensional plane strain setting. Details of the implementation are presented hereafter.

### 3.1. *Cohesive law*

Failure of the particle–matrix interface is modelled using four-noded cohesive elements which obey the bilinear traction-separation law described by Geubelle and Baylor [20] and shown in Figure 2. Under Mode I loading (Figure 2a), the two surfaces of the cohesive element begin to separate (A), with a constant initial stiffness. Once the interface strength, $\sigma_{\max}$, is reached, the interface becomes weaker with increasing separation (B), until achieving the critical separation $\Delta n_c$, at which point failure is complete and the interface can no longer sustain tractions (C). Unloading and reloading prior to complete failure

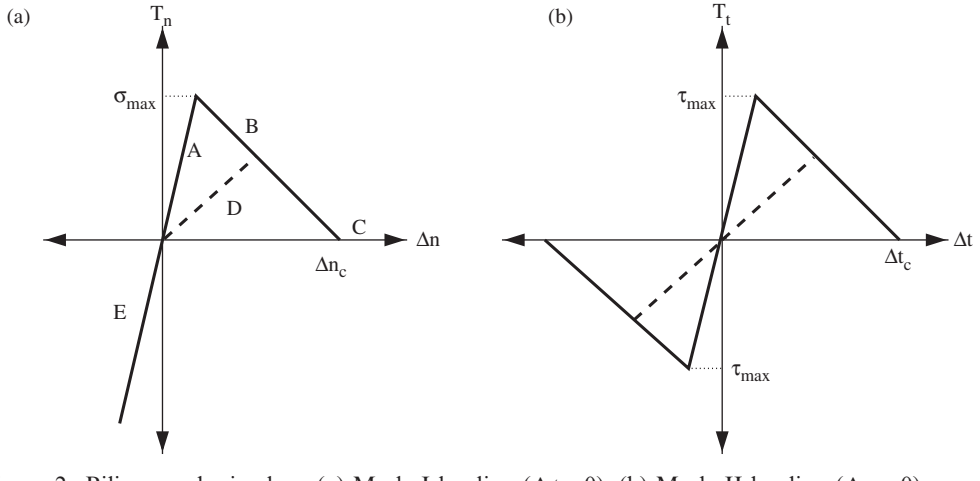


Figure 2. Bilinear cohesive law. (a) Mode I loading ($\Delta t = 0$). (b) Mode II loading ($\Delta n = 0$).

Downloaded By: [University of Illinois] At: 17:27 29 September 2008

follow the damaged path (D). Negative normal displacement results in a stiff response with no accumulation of damage (E), which serves as a simple penalty response to possible contact or interpenetration. The model is similar for the case of Mode II loading (Figure 2b), except that the response is antisymmetric. The two modes are coupled through a state variable, the interface damage parameter $S$.

The normal ($T_n$) and tangential ($T_t$) cohesive tractions are related to the normal ($\Delta n$) and tangential ($\Delta t$) displacement jumps through

$$T_n = \begin{cases} \dfrac{\sigma_{\max}}{S_{\text{init}}} \dfrac{S}{1-S} \dfrac{\Delta n}{\Delta n_c} & \text{for } \Delta n \geq 0, \\ \dfrac{\sigma_{\max}}{1-S_{\text{init}}} \dfrac{\Delta n}{\Delta n_c} & \text{for } \Delta n < 0, \end{cases} \tag{27}$$

$$T_t = \frac{\tau_{\max}}{S_{\text{init}}} \frac{S}{1-S} \frac{\Delta t}{\Delta t_c}, \tag{28}$$

where $S$ is the monotonically decreasing interface damage parameter, representing the remaining capacity of the local interface to sustain cohesive tractions,

$$S = \left\langle \left\langle 1 - \sqrt{\left(\frac{\Delta n}{\Delta n_c}\right)^2 + \left(\frac{\Delta t}{\Delta t_c}\right)^2} \right\rangle \right\rangle \tag{29}$$

when $\Delta n$ is positive. In (29), $\langle\langle a \rangle\rangle = a$ if $a > 0$ and $\langle\langle a \rangle\rangle = 0$ otherwise. No damage is permitted to accumulate in the presence of a compressive normal displacement ($\Delta n < 0$). An *undamaged* interface has $S = S_{\text{init}}$, a *damaged* interface has $S_{\text{init}} > S > 0$, and for a *fully failed* interface $S = 0$. $S_{\text{init}}$ is chosen to be 0.98 for these studies. The choice of $S_{\text{init}} < 1$, which defines an intrinsic cohesive law, eliminates numerical instabilities associated with rigid elements [21]. An adaptive load-stepping scheme is used to capture the failure process accurately.

### 3.2. *Applying boundary conditions*

In order to apply periodic boundary conditions, we require a periodic mesh. Periodicity is enforced by assigning the same equation number to corresponding nodes on opposite boundaries. As indicated by (18) the macroscopic strain term acts as a loading term.

In the small strain finite element setting, the minimal kinematic boundary conditions (21) become

$$2|\Theta|\boldsymbol{E} = \boldsymbol{L}\boldsymbol{d}, \tag{30}$$

where

$$\boldsymbol{L} = \frac{\partial}{\partial \boldsymbol{d}} \left[ \int_{\partial\Theta} \left( u_i n_j + u_j n_i \right) \mathrm{d}\Theta \right]$$

Downloaded By: [University of Illinois] At: 17:27 29 September 2008

and $\boldsymbol{d}$ is the nodal displacement vector. Mesarovic and Padbidri [14] report enforcing (30) through the direct method. Based on their suggestion we adopt here an alternative method based on Lagrange multipliers, defining the constraint equation as

$$\boldsymbol{g}(\boldsymbol{d}) = \boldsymbol{L}\boldsymbol{d} - 2|\Theta|\boldsymbol{E}, \tag{31}$$

and solving the resulting augmented system $\bar{\boldsymbol{K}}\bar{\boldsymbol{d}} = \bar{\boldsymbol{R}}$,

$$\begin{bmatrix} \boldsymbol{K} & \boldsymbol{L}^T \\ \boldsymbol{L} & \boldsymbol{0} \end{bmatrix} \begin{Bmatrix} \boldsymbol{d} \\ \boldsymbol{\lambda} \end{Bmatrix} = \begin{Bmatrix} \boldsymbol{0} \\ 2|\Theta|\boldsymbol{E} \end{Bmatrix}. \tag{32}$$

In (32), $\boldsymbol{\lambda}$ contains the Lagrange multipliers, three additional degrees of freedom in the two-dimensional problem. The three fixed degrees of freedom, imposed to eliminate rigid body translation and rotation, are handled through the standard partitioning of the problem into free and prescribed degrees of freedom.

Downloaded By: [University of Illinois] At: 17:27 29 September 2008

### 3.3. *Problem definition*

To examine the differences and similarities between periodic and minimal kinematic boundary conditions, we perform simulations on periodic two-dimensional particle packs with particle diameter $d$ ranging from 80 to 100 μm. The pack generation and meshing procedure are described in detail by Matouš et al. [22]. Packs are generated using a packing algorithm [23] which starts from randomly generated seeds, allowing the generation of a range of packs with similar volume fraction but different packing arrangements. A high quality periodic mesh, with sufficient mesh refinement to satisfy requirements on the number of volumetric elements between particles, and with cohesive elements inserted at all particle–matrix boundaries, is created using the T3D meshing tool [24], and shown in Figure 3. Volumetric material properties and cohesive interface properties are given in Tables 1 and 2 respectively. Note the large stiffness mismatch between the inclusions and the moderately compressible matrix. The interface properties are chosen such that failure occurs within the limits of small strain.

To study the undamaged stiffness, we use meshes with volumetric elements only, and consider packs of size $L = 400$, 800 and 1200 μm, as detailed in Table 3. Table 4 summarizes the six packs containing cohesive elements, which are used to examine the development of localization. The cohesive packs are of size $L = 800$ μm (i.e. about eight times the particle diameter), since this choice offers a compromise between accuracy of results and computational cost [25]. Each cohesive pack is labelled for reference when evaluating results.

The mesh generation tool allows particles to be cut by the boundaries, facilitating a closer periodic pack. However, under MKBC, once a particle on the boundary debonds the solution is no longer unique. For that reason, we consider only packs which have no particles intersecting the boundaries in the localization study. Note that periodicity of the mesh is not required for MKBC.

A focus of this work is the investigation of the performance of periodic boundary conditions in capturing localization that is not aligned with the periodic boundaries.

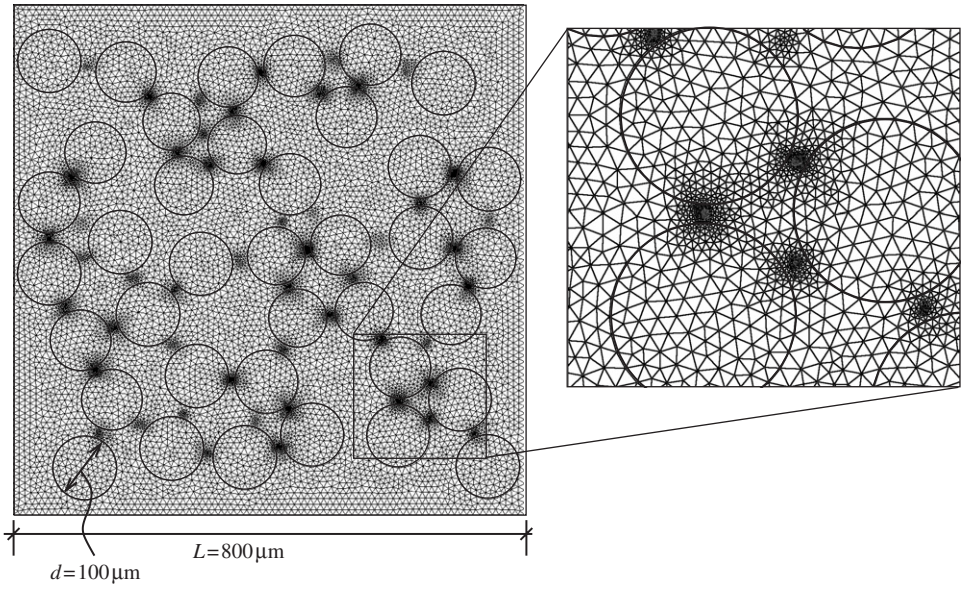


Figure 3. Finite element discretization of one of the microstructures used in this study with inclusion volume fraction of 43.76%. The inset shows in more detail the areas of refinement between particles.

Table 1. Volumetric material properties.

| Constituent | $E$ [MPa] | $\nu$ |
|---|---|---|
| Particles | 3700 | 0.1433 |
| Binder | 2.4 | 0.4 |

Table 2. Cohesive interface properties.

| Property | Symbol | Value |
|---|---|---|
| Interface strength [MPa] | | |
| Normal | $\sigma_{\max}$ | 0.05 |
| Tangential | $\tau_{\max}$ | 0.05 |
| Critical opening displacement [μm] | | |
| Normal | $\Delta n_c$ | 0.75 |
| Tangential | $\Delta t_c$ | 0.75 |

In order to compare results from the same loading case applied at different angles relative to the sample, all stresses and strains will be shown in rotated coordinates, following the convention illustrated in Figure 4. The macroscopic strains are transformed using the familiar expressions

Downloaded By: [University of Illinois] At: 17:27 29 September 2008

Table 3. Pack specifications: packs without cohesive elements.

| Pack size [μm] | Number of packs | Number of particles | Volume fraction [%] | Particle diameter [μm] | PBC average modulus [MPa] | MKBC average modulus [MPa] |
|---|---|---|---|---|---|---|
| 400 | 10 | 9–10 | 44.7–49.1 | 80.56–100.00 | $8.06 \pm 1.08$ | $6.99 \pm 0.78$ |
| 800 | 10 | 34–41 | 38.9–46.9 | 80.06–100.00 | $7.73 \pm 0.32$ | $7.19 \pm 0.25$ |
| 1200 | 10 | 77–91 | 38.3–45.8 | 80.88–100.00 | $7.87 \pm 0.22$ | $7.41 \pm 0.21$ |

Table 4. Pack specifications: packs containing cohesive elements.

| Pack | Number of particles | Volume fraction [%] | Largest particle diameter [μm] | Smallest particle diameter [μm] | Average particle diameter [μm] |
|---|---|---|---|---|---|
| A | 38 | 43.76 | 100.00 | 89.78 | 96.81 |
| B | 38 | 46.34 | 100.00 | 88.47 | 96.44 |
| C | 39 | 47.56 | 100.00 | 82.85 | 96.45 |
| D | 40 | 48.78 | 100.00 | 81.84 | 96.79 |
| E | 39 | 44.03 | 100.00 | 86.36 | 96.12 |
| F | 39 | 44.52 | 100.00 | 84.14 | 96.66 |

$$\begin{aligned}
\bar{\varepsilon}_{\hat{1}\hat{1}} &= \frac{\bar{\varepsilon}_{11} + \bar{\varepsilon}_{22}}{2} + \frac{\bar{\varepsilon}_{11} - \bar{\varepsilon}_{22}}{2}\cos 2\theta + \bar{\varepsilon}_{12}\sin 2\theta, \\
\bar{\varepsilon}_{\hat{2}\hat{2}} &= \frac{\bar{\varepsilon}_{11} + \bar{\varepsilon}_{22}}{2} - \frac{\bar{\varepsilon}_{11} - \bar{\varepsilon}_{22}}{2}\cos 2\theta + \bar{\varepsilon}_{12}\sin 2\theta, \\
\bar{\varepsilon}_{\hat{1}\hat{2}} &= -\frac{\bar{\varepsilon}_{11} - \bar{\varepsilon}_{22}}{2}\sin 2\theta + \bar{\varepsilon}_{12}\cos 2\theta,
\end{aligned} \tag{33}$$

with similar relations for the coordinate transformation of the macroscopic stresses. In all cases, the coordinate transformation recovers the principal strains, $\bar{\varepsilon}_{\hat{1}\hat{1}}$ and $\bar{\varepsilon}_{\hat{2}\hat{2}}$, with $\bar{\varepsilon}_{\hat{1}\hat{2}} = 0$.

### 3.4. *Comparison of fluctuating displacement fields*

The fluctuating displacement fields and macroscopic stress–strain response obtained from a simple four particle unit cell are compared in Figure 5. As might be expected for a unit cell which is unlikely to be representative, the two curves do not coincide. The horizontal component of the fluctuating displacement is shown on the microstructures in Figure 5b and c. In the displaced shapes, the contrast between the periodicity of PBC and the minimal constraint of MKBC is clear. The relative rigid displacement between the two cases has been subtracted from the result to allow for direct comparison. Note that the corners of the MKBC domain experience extreme values while those of the PBC domain experience the average value of the fluctuating displacement field.

Downloaded By: [University of Illinois] At: 17:27 29 September 2008

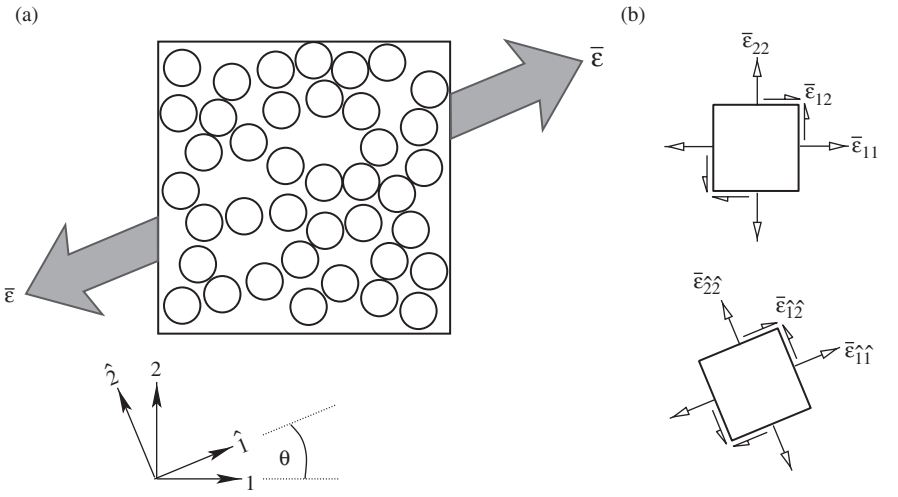


Figure 4. Schematic illustrating coordinate numbering conventions. (a) A sample pack is loaded with uniaxial macroscopic strain $\bar{\boldsymbol{\varepsilon}}$ at an angle $\theta$ from the horizontal. The original coordinate system, which is aligned with the boundaries of the pack, is denoted by indices 1 and 2. The rotated coordinate system, aligned with the direction of loading, is denoted by indices $\hat{1}$ and $\hat{2}$. (b) Material elements show strains expressed in the pack coordinates (top) and in the rotated coordinates (bottom).

## 4. Shear loading

### 4.1. *Shear stiffness*

Mesarovic and Padbidri [14] observed a higher shear modulus from periodic boundary conditions (PBC) than from minimal kinematic boundary conditions (MKBC). In addition, MKBC converged to a smaller RVE size than PBC. Before moving to the case with damage, we revisit their study for a two-dimensional particulate composite with significant stiffness mismatch, computing the undamaged shear stiffness for 10 packs at each of three different sizes under both periodic and minimal kinematic boundary conditions. Table 3 summarizes the statistics of the pack geometries. Figure 6 shows the shear modulus, $\bar{\mu}_{12} = \bar{\sigma}_{12}/\bar{\varepsilon}_{12}$, plotted against the normalized pack size $L/d$. Filled triangles indicate PBC results, while MKBC results are plotted as diamonds. For clarity, the two datasets are offset slightly to the left and right of the RVE size at which they were computed. For each dataset, the average and standard deviation has been computed and listed in Table 3.

To place the results in context, Figure 6(a) is scaled out to show the theoretical upper and lower bounds on the shear modulus; the results are shown in detail in Figure 6(b). The dotted lines on the graphs indicate theoretical bounds calculated from a simple rule of mixtures analysis, the Voigt and Reuss bounds. The solid lines denote the Hashin–Shtrikman bounds, calculated from the principle of energy minimization. The width of the bounds is a consequence of the mismatched material stiffnesses listed in Table 1. The results are close to the lower bounds and, in Figure 6a, the lower bounds as well as the data set are collapsed close to the $x$-axis and are indistinguishable from one another. The self-consistent scheme [26] predicts a shear stiffness of 12.7 MPa, close to the theoretical lower bounds.

Downloaded By: [University of Illinois] At: 17:27 29 September 2008

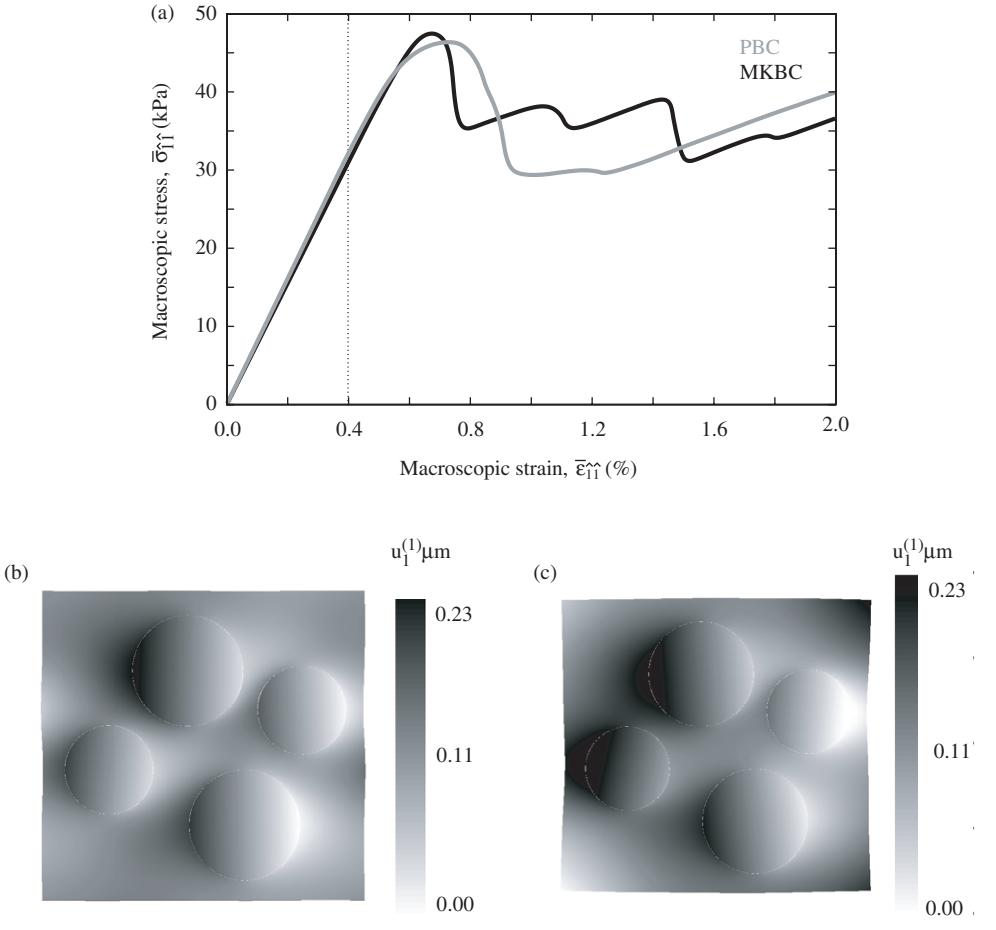


Figure 5. Comparison of fluctuating displacement fields for a simple four-particle pack under uniaxial strain aligned with the cell boundaries. (a) Macroscopic stress–strain responses. At 0.4% strain, the fluctuating displacement field $u_1^{(1)}$ is plotted on the deformed shape with displacements magnified 10 times for (b) PBC and (c) MKBC.

The results shown in Figure 6b are in general agreement with those obtained by Mesarovic and Padbidri [1] for a polycrystalline material. All stiffness results fall between the Hashin–Shtrikman theoretical bounds. The PBC stiffness is always higher than the MKBC stiffness for the same pack. Notice that the stiffest PBC response arises from the pack which has the stiffest MKBC response (points 1 and 2 respectively in Figure 6b, from a pack with higher than average inclusion volume fraction). With increasing pack size $L$, the scatter associated with both boundary conditions decrease, and the stiffness value predicted by MKBC appears to converge faster than its PBC counterpart. The difference between the two results also converges with increasing pack size. For packs with $L/d = 12$, the PBC stiffness is consistently 6–7% greater than the MKBC stiffness, contrasting with differences of 7–25% for $L/d = 4$.

Downloaded By: [University of Illinois] At: 17:27 29 September 2008

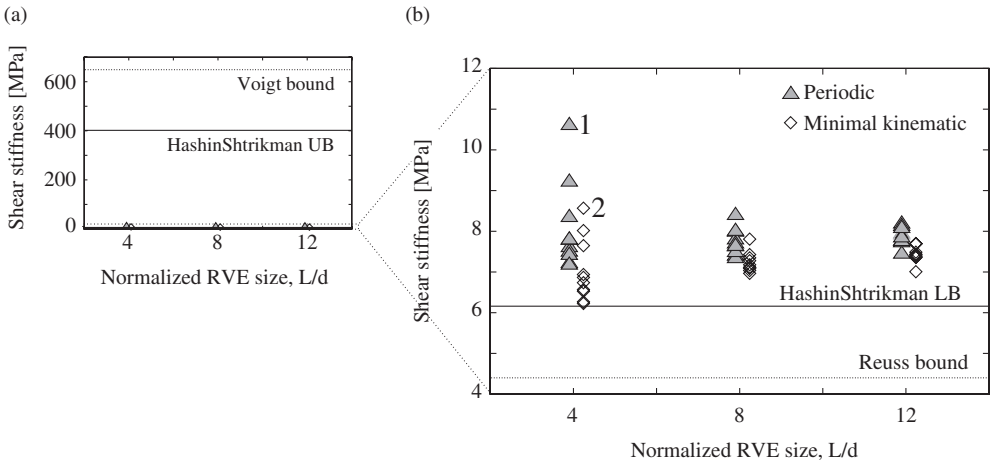


Figure 6. Effect of RVE size $L$ (normalized by the particle diameter) on the shear modulus of the undamaged pack, for PBC (triangles) and MKBC (diamonds). (a) shows upper and lower bounds on the shear modulus, (b) is scaled to the data and shows only the lower bounds.

Downloaded By: [University of Illinois] At: 17:27 29 September 2008

### 4.2. *Shear loading with damage*

To investigate the possible restriction of localization under periodic boundary conditions, hypothesized by Mesarovic and Padbidri [14], we subject a sample pack to a macroscopic shear strain, $\bar{\varepsilon}_{11} = \bar{\varepsilon}_{22} = 0$, $\bar{\varepsilon}_{12} = 0.02$. Figure 7a shows the macroscopic stress–strain response and the evolution of cohesive damage and cohesive failure. The stress–strain curve relates the principal stress $\bar{\sigma}_{\hat{1}\hat{1}}$ to the principal strain $\bar{\varepsilon}_{\hat{1}\hat{1}}$. The coordinate transformation is necessary since plotting $\bar{\sigma}_{12}$ against $\bar{\varepsilon}_{12}$ masks the nonlinearity of the solution. The imposed macroscopic shear strain is equivalent to the principal strain state $\bar{\varepsilon}_{\hat{1}\hat{1}} = 0.02$, $\bar{\varepsilon}_{22} = -0.02$, $\bar{\varepsilon}_{\hat{1}\hat{2}} = 0$.

In Figures 7–13, results obtained with PBC are denoted by grey lines, while those corresponding to MKBC are shown with black lines. The solid curves indicate the stress response, shown on the left axis. The fraction of the cohesive interface which has experienced damage is given by dashed curves, while the fraction of the cohesive interface which has failed completely is given by dotted curves. Both the dashed and dotted curves refer to the right axis of the graph. The damaged fraction of the interface is computed by calculating the length of all cohesive elements for which $S < S_{\text{init}}$, normalized by the total length of cohesive elements, i.e. the sum of all particle boundaries. Similarly, the failed fraction of the cohesive interface arises from cohesive elements for which $S = 0$.

The constitutive response observed in Figure 7a is initially linear, becoming nonlinear as a result of the onset of damage in cohesive elements (at about 0.2% principal strain). The onset of failure in cohesive elements (occurring at about 0.4% principal strain) coincides with the local maximum of the macroscopic stress. A plateau in the stress–strain response, as damage and failure accumulate, is followed by a stiffening response as the damage saturates. Notice that half of the cohesive interfaces remain undamaged, since they are shielded by the compressive strain.

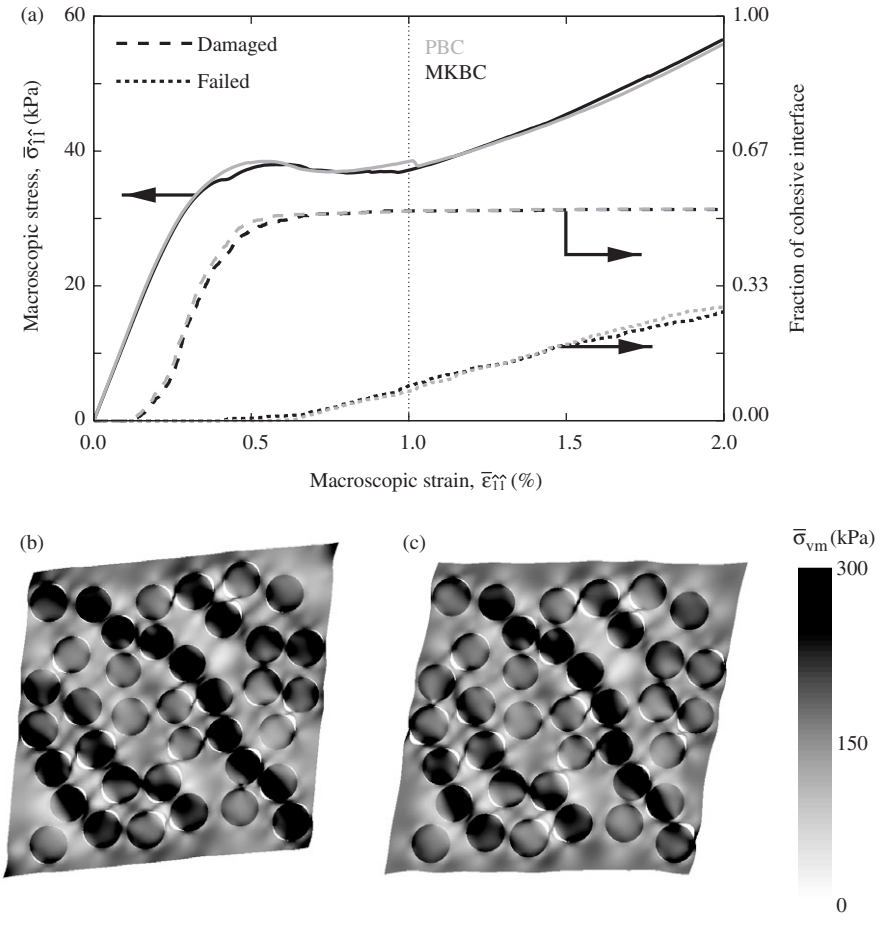


Figure 7. Macroscopic shear loading (pack A). (a) The macroscopic principal stress (solid line) is plotted against the macroscopic principal strain on the same graph as the damage (dashed) and failure (dotted) evolution curves. The von Mises stress distribution at $\bar{\varepsilon}_{\hat{1}\hat{1}} = 1\%$ (vertical dotted line in (a)) is plotted on the deformed packs with displacements magnified 10 times for (b) periodic and (c) minimal kinematic boundary conditions.

Figure 7b and c show von Mises stress fields plotted on deformed packs at 1% principal strain. The microstructures show considerable distributed damage, but no localization. Since localization is absent, the microstructures look similar at all loading stages, with only the intensity of the von Mises stress field and the degree of cohesive interface opening increasing as the applied macroscopic strain increases. Figure 7b has periodic boundary conditions, which are evident in comparison of the deformed profiles of the left and right edges. Figure 7c presents the displaced shape of the pack under minimal kinematic boundary conditions. To eliminate rigid body motion, the bottom left node is fixed in both directions, and the bottom right node is fixed in the vertical direction. The deformed shapes under these two different boundary conditions are therefore equivalent except for a rigid body rotation.

Downloaded By: [University of Illinois] At: 17:27 29 September 2008

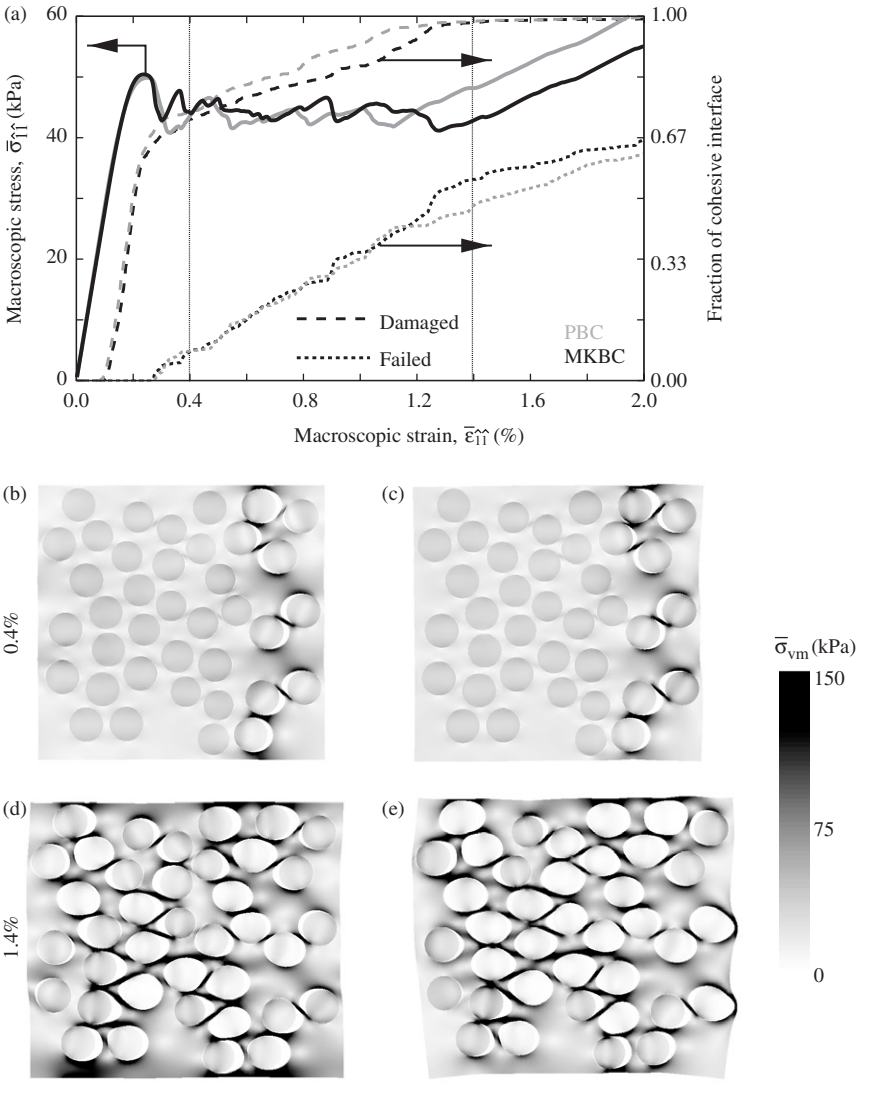


Figure 8. Macroscopic uniaxial strain (pack B). (a) Constitutive response and damage evolution. At 0.4% strain, the deformed microstructures under (b) periodic (PBC) and (c) minimal kinematic (MKBC) boundary conditions have formed localization bands. At 1.4% strain, (d) PBC and (e) MKBC both exhibit extensive damage, and many particles have completely unloaded, making them difficult to distinguish from voids. Displacements are magnified 10 times in all microstructures, which are shown with the von Mises stress distribution.

The macroscopic responses and the stress distributions in the microstructures show a marked similarity. The initial stiffness of PBC is fractionally higher than that of MKBC, and PBC shows small local increases in stress in the corners of the domain, due to the additional constraint of periodicity. The compressive principal strain inhibits the localization of damage equally for both methods.

Downloaded By: [University of Illinois] At: 17:27 29 September 2008

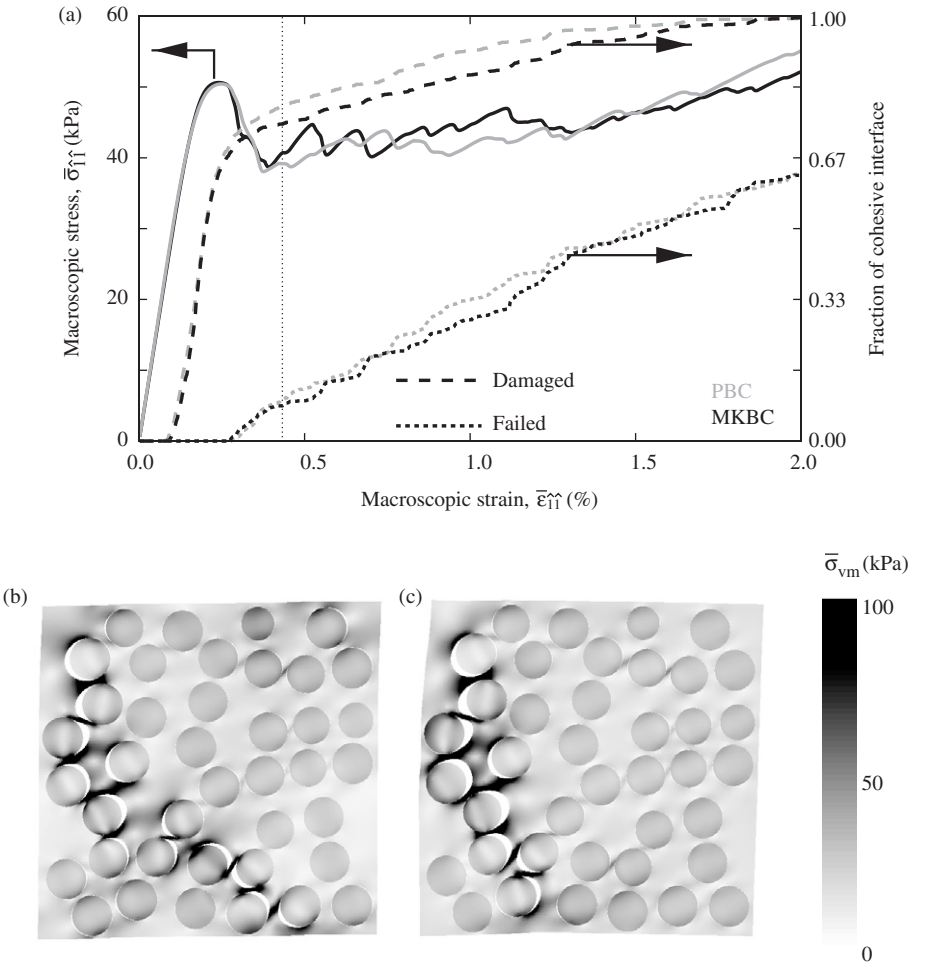


Figure 9. Macroscopic uniaxial strain at 22.5° (pack D). (a) Principal stress is plotted against principal strain, with damage evolution curves on the same graph. The von Mises stress distribution is plotted on deformed microstructures for $\bar{\varepsilon}_{\hat{1}\hat{1}} = 0.4$ under (b) periodic and (c) minimal kinematic boundary conditions, with displacements magnified by a factor of 10.

## 5. Uniaxial strain loading

### 5.1. *Uniaxial loading aligned with cell boundaries*

For the shear loading case discussed in Section 4, localization was inhibited by the presence of a compressive principal strain. In order to promote the appearance of localization, we impose a uniaxial strain on the microstructure. The uniaxial macroscopic strain is first applied in the 1-direction ($\theta = 0°$), aligned with the cell boundaries. This loading case, in which PBC do not limit localization, will serve as a control case for future comparison. Figure 8a shows the macroscopic response, which differs significantly from the response under shear loading. As was the case for shear loading, the first deviation

Downloaded By: [University of Illinois] At: 17:27 29 September 2008

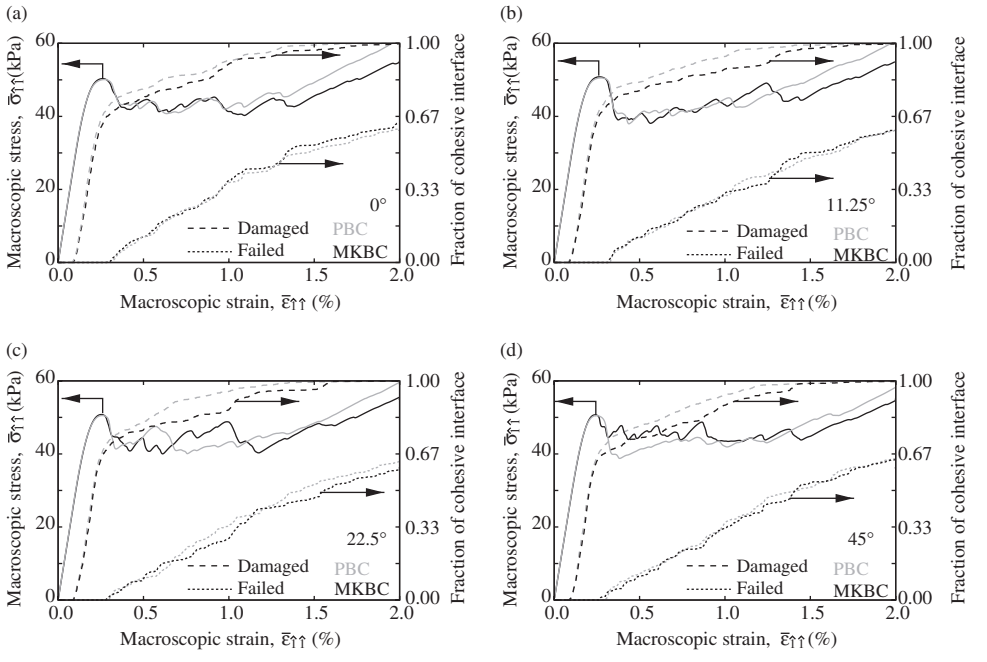


Figure 10. Macroscopic uniaxial strain (pack C). Constitutive response in the principal direction, as well as damage and failure evolution curves, are shown for loading at (a) 0°, (b) 11.25°, (c) 22.5° and (d) 45° to the pack coordinates.

from linearity in the stress–strain curve is correlated with the onset of damage, the peak stress is coincident with the first failure of cohesive interfaces, and the final slope is attained once the damage has saturated. Unlike the shear case, the entire cohesive interface is eventually damaged, and two-thirds of the cohesive interface fails completely. The stress–strain response following the initial peak is jagged, an artefact of the non-smooth bilinear cohesive law, and the explicit finite element formulation. The deformed microstructure shows the presence of localization bands.

There is more variation between the responses under different boundary conditions than was observed previously. While the initial slope and the peak stress are similar, the specific profiles of the stress–strain curves are different. The same final slope is attained under both boundary conditions, but the MKBC curve shows a lower stress for the same strain than the PBC curve. The differences between the constitutive responses can be elucidated by considering the damage evolution curves. From 0.3% to 1.2% applied strain, the periodic case has a higher fraction of damaged interface than the minimal kinematic case, with a correspondingly lower stress. From 1.2% applied strain onwards, the minimal kinematic case has a much higher fraction of failed interface, corresponding to the lower stress in that region.

Considering the deformed microstructures gives us additional insight. At 0.4% applied strain (Figure 8b and c), both cases have formed a localization band near the right edge of the domain. The formation of the band corresponds with the initial drop-off in the macroscopic stress at around 0.3% strain. The von Mises stress distributions

Downloaded By: [University of Illinois] At: 17:27 29 September 2008

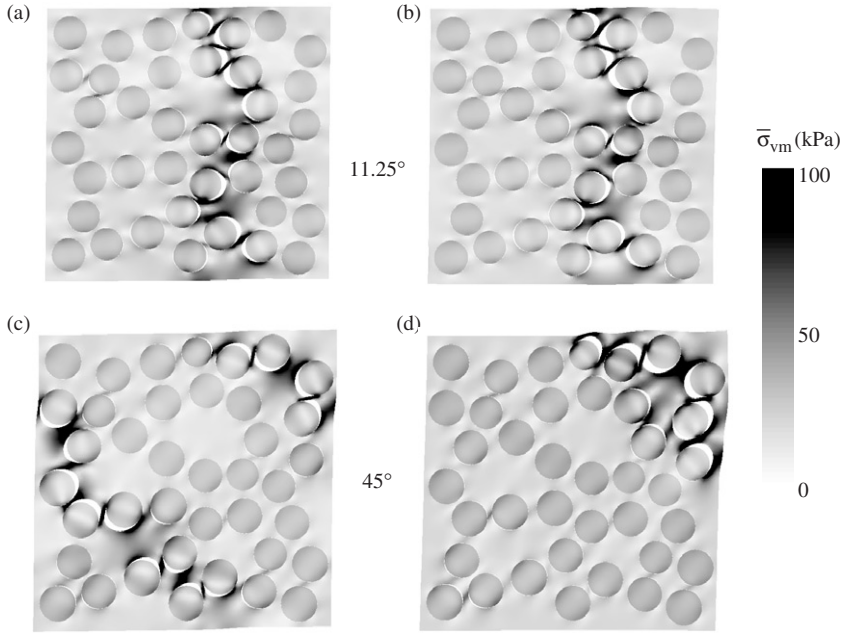


Figure 11. Macroscopic uniaxial strain (pack C). The von Mises stress distribution is plotted on deformed microstructures at $\bar{\varepsilon}_{\hat{1}\hat{1}} = 0.4\%$, with displacements magnified 10 times. Loading at $\theta = 11.25^\circ$ for (a) PBC and (b) MKBC. Loading at $\theta = 45^\circ$ for (c) PBC and (d) MKBC.

and displaced shapes are very similar between the two cases, although the differing constraints around the boundary give rise to slightly different stress concentration and deformation patterns in the vicinity of the localization band. Each subsequent dip in the stress–strain curves corresponds to the formation of another localization band or semi-band. For this reason, the variance between the loading cases is not significant in this region, since the random statistics of particle arrangement and interactions will trigger slightly different localization events. At 1.4% applied strain (Figure 8d and e), there is distributed damage throughout the domain, with the individual localization bands no longer discernible. With no further undamaged cohesive interfaces, the stress in the domain begins to increase once more. The deformed microstructures at 1.4% applied strain show that the additional failure possible in the minimal kinematic case is due to the compliance of matrix ligaments around the boundary, which bulge considerably to accommodate the applied strain, indicating that MKBC may not apply sufficient constraint to the boundary when debonding is present.

It should be noted that these results are for a model which does not allow damage or failure of the matrix material. Were matrix failure permitted, the pack would fail completely long before the stress capacity began to increase again. The formation of multiple localization bands might therefore be viewed as an artefact of the linearly increasing imposed macroscopic strain. In a fully coupled multiscale simulation, the macroscopic strain field would be altered as a consequence of damage localization.

Downloaded By: [University of Illinois] At: 17:27 29 September 2008

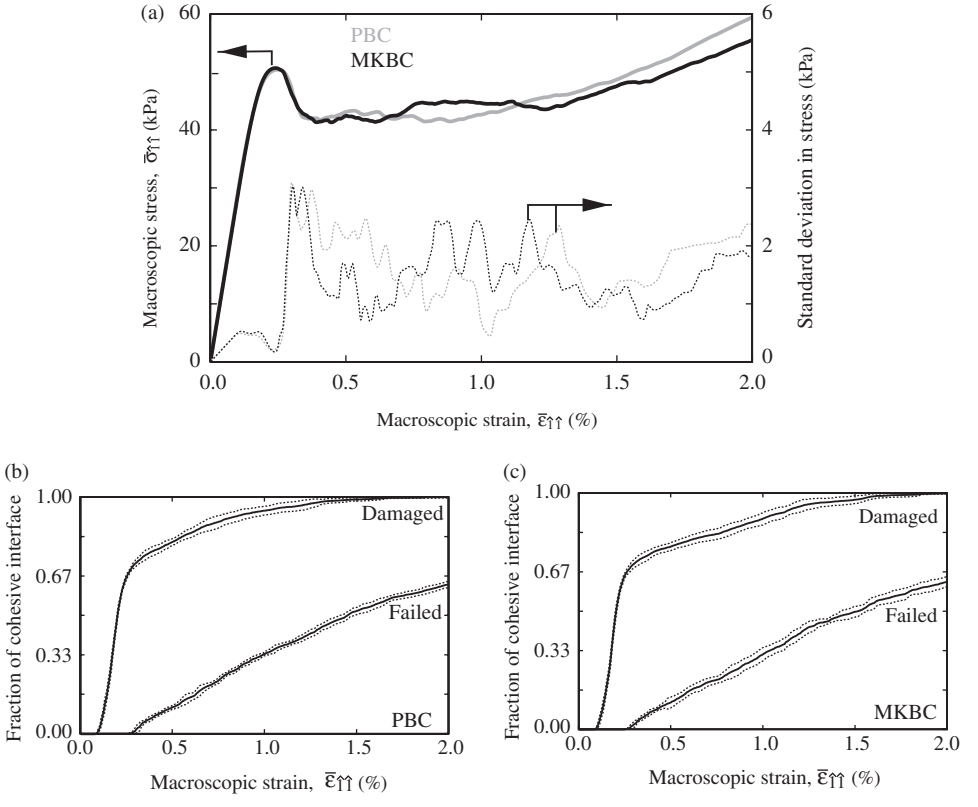


Figure 12. Averages (thick curves) and standard deviations (dotted curves) calculated for results from six packs under macroscopic uniaxial strain at 22.5°. (a) Macroscopic stress–strain response. (b) PBC damage and failure evolution curves with the standard deviation indicated as error bounds. (c) MKBC damage and failure evolution curves.

### 5.2. *Uniaxial loading at an angle to cell boundaries*

As shown in the previous section, periodic boundary conditions can capture localization as effectively as minimal kinematic boundary conditions under uniaxial strain with loading aligned with the axis of the domain. Consider now the case where the macroscopic loading direction is not aligned with the pack boundaries. Figure 9 shows the response to uniaxial strain loading at $\theta = 22.5°$. The macroscopic response (Figure 9a) is basically the same as for the $\theta = 0°$ case, contradicting the assumption that periodic boundary conditions are not able to capture localization if that localization is not inherently periodic. Looking at the PBC microstructure in Figure 9b, we can see how localization is achieved. A primary localization band, approximately vertical, joins a secondary band at 45°. Together, these bands give an average response at 22.5°. The bands reach the cell boundaries in the top left and bottom right corners, and can thus satisfy periodicity. Note that the region of high stress in the matrix at the bottom right corresponds with a similar region in the top left corner. The need to accommodate periodicity leads thus to more extensive damage under PBC than MKBC, which is evident in the macroscopic damage curves, with the periodic

Downloaded By: [University of Illinois] At: 17:27 29 September 2008

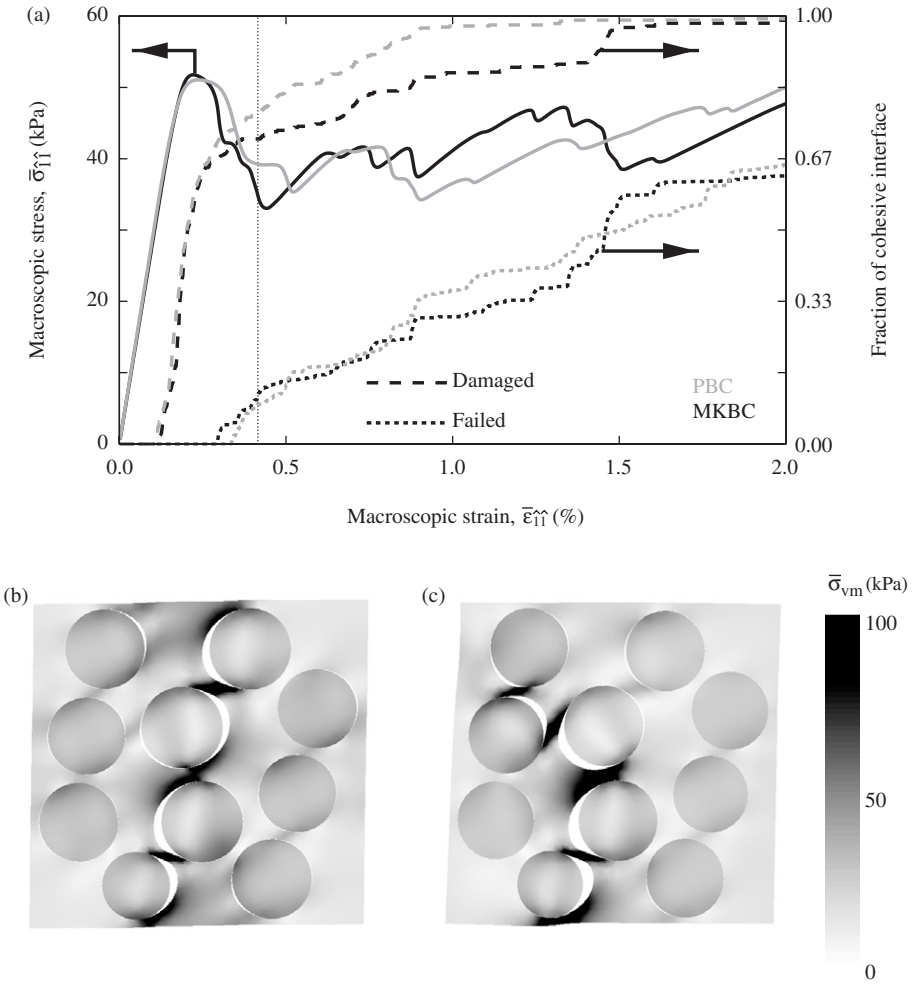


Figure 13. Macroscopic uniaxial strain at 22.5° on a small pack. (a) Principal stress is plotted against principal strain, with damage evolution curves on the same graph. The von Mises stress distribution is plotted on deformed microstructures for $\bar{\varepsilon}_{\hat{1}\hat{1}} = 0.4\%$ under (b) periodic and (c) minimal kinematic boundary conditions, with displacements magnified by a factor of 10.

case showing more damage and failure at most stages of the loading. In contrast, the MKBC microstructure, Figure 9c, shows only a single band of localization, and the boundary conditions permit bulging of the left edge during the localization. However, the difference in the type and extent of damage does not appear to affect the macroscopic response significantly. The lower MKBC curve after 1.5% strain is due to the reduced constraint on particle failure close to the boundary, resulting in extra straining of narrow matrix ligaments without additional damage, as discussed previously. Note that only weak localization is studied, since we model only decohesion and not matrix failure.

Downloaded By: [University of Illinois] At: 17:27 29 September 2008

The ability of the periodic boundary conditions to capture localization is consistent across all loading angles. Figure 10 shows the macroscopic stress–strain and damage evolution responses for a range of loading angles from $\theta = 0^\circ$ to $\theta = 45^\circ$. For clarity, the responses are plotted separately for each loading case. In all cases, the curves are very similar, with the same initial stiffness and the same stress and strain values at the initial peak. The key features of the earlier results are also present. In all the curves, MKBC damage lags PBC damage due to the somewhat unphysical constraints imposed by periodicity. While the slope in the final stages of the stress–strain curve is the same for both boundary conditions, the MKBC curve is consistently lower than the PBC curve in that region.

Figure 11 shows the deformed microstructures for loading angles of $11.25^\circ$ and $45^\circ$. When $\theta = 11.25^\circ$ (Figure 11a and b) the specific pack geometry favours a wide localization band, satisfying the periodic requirement naturally. The localization bands form in the same location for both boundary conditions, and the deformed microstructures are nearly identical. This similarity can also be seen in the very close correspondence between the first half of the stress–strain curves in Figure 10b. Under uniaxial loading at $45^\circ$ (Figure 11c and d) the localization behaviour is very different for the two boundary conditions. The PBC microstructure shows two localization bands, which together satisfy the requirement of periodicity. The MKBC cell localizes in the top right corner, the same location as localization initiated under PBC. Since the area of localization is very close to the domain boundaries, further strain is accommodated by excessive straining of the localized region, rather than by additional straining of the remainder of the microstructure. This is also apparent in the stress–strain curve, Figure 10d, where a higher macroscopic stress under MKBC results from the distortion of the microstructure. For all the microstructures considered, the specific packing geometry plays a large role in the nature of the localization and macroscopic stress–strain response.

Statistical comparison of results for uniaxial loading at $\theta = 22.5^\circ$ shows consistency across different pack geometries. The averages (solid curves) and standard deviations (dotted curves) of the macroscopic stress response in Figure 12a are very similar for the two loading conditions. The standard deviation is at most 5% of the average stress and has a very similar profile for both PBC and MKBC. Note that the minimum value of standard deviation occurs at the peak in the macroscopic stress–strain response, suggesting that the values at the peak (i.e. damage nucleation) are characteristic for the volume fraction and material properties, and are not substantially dependent on the details of the pack microstructure. Notice however that damage propagation is strongly influenced by cell arrangement. Figure 12b shows the damage evolution (top curve) and failure evolution (bottom curve) averages and error bounds for PBC, while Figure 12c shows the same results for MKBC. The narrow error bounds indicate repeatability of the data. The damage evolution curve is slightly higher for PBC than MKBC, consistent with the observations from individual results, while the failure evolution curves are nearly identical.

Finally, to demonstrate that the ability of PBC to capture weak localization under non-periodic loading conditions is not simply a consequence of using a sufficiently large unit cell, Figure 13 shows results from uniaxial loading at $\theta = 22.5^\circ$ applied to a base cell of size $L = 400\,\mu m$. There is a slight difference between the stress–strain peaks in the two responses, and there is somewhat more variation between the curves in Figure 13a than was observed for the larger base cells, but to a large extent the two boundary conditions agree. As was the case for $\theta = 11.25^\circ$, the localization band is wide in order to accommodate the non-periodic localization under periodic constraints.

Downloaded By: [University of Illinois] At: 17:27 29 September 2008

## 6. Conclusions

We have compared the behaviour of a particulate composite system under periodic boundary conditions and under the minimal kinematic boundary conditions introduced by Mesarovic and Padbidri [14]. For an undamaged material system, the computed shear stiffness is 6–7% higher with periodic boundary conditions than with minimal kinematic boundary conditions, consistent with the results obtained by Mesarovic and Padbidri. In a system where interfacial damage is modelled, periodic boundary conditions successfully capture weak localization associated with the particle debonding process even when that weak localization is not aligned with the domain axes. For some pack geometries and some loading cases, the additional constraint of periodicity is satisfied by the formation of more than one band of partial localization. Characteristic features of the homogenized solution, including the initial slope, the initial peak, and evolution of damage and failure, are similar for the two boundary conditions across multiple packs.

The results suggest that the multiscale scheme based on periodic boundary conditions, which is supported by a wealth of theoretical development and is attractive because of its mathematical tractability, can be used even in the case of off-axis damage localization. The multiscale scheme based on MKBC presents the key advantage of not requiring periodic RVEs, and can therefore be applied to a wider range of microstructures, especially those extracted directly from actual micrographs.

The multiscale scheme based on minimal kinematic boundary conditions does not perform well when particles are too close to the boundaries. The integral constraint is then satisfied by excessive straining of a narrow ligament, rather than by deformation of the entire domain. The introduction of a penalty term in the integral boundary condition may improve the performance of this method.

Downloaded By: [University of Illinois] At: 17:27 29 September 2008

## Acknowledgements

This work was supported by the Center for Simulation of Advanced Rockets (CSAR) under contract number B523819 by the US Department of Energy. Karel Matouš would also like to acknowledge support from ATK/Thiokol (ATK-21316), with J. Thompson and Dr I.L. Davis serving as program monitors.

## References

[1] T. Kanit, S. Forest, I. Galliet et al., Int. J. Solids Struct. 40 (2003) p.3647.
[2] R. Pyrz, Mat. Sci. Eng. A Struct. 177 (1994) p.253.
[3] J. Zeman and M. Šejnoha, J. Mech. Phys. Solids 49 (2001) p.69.
[4] N.C. Kumar, K. Matouš and P. H. Geubelle, Comp. Mater. Sci. 42 (2008) p.352.
[5] S. Swaminathan and S. Ghosh, J. Compos. Mater. 40 (2006) p.605.
[6] J.M. Guedes and N. Kikuchi, Comput. Methods Appl. Mech. Engng. 83 (1990) p.143.
[7] S. Ghosh, K. Lee and S. Moorthy, Int. J. Solids Struct. 32 (1995) p.27.
[8] J. Fish, K. Shek, M. Pandheeradi et al., Comput. Methods Appl. Mech. Engrg. 148 (1997) p.53.
[9] K. Matouš and P. Geubelle, Int. J. Numer. Meth. Engng. 65 (2006) p.190.
[10] A. Bensoussan, J.L. Lions and G. Papanicolaou, *Asymptotic Analysis for Periodic Structures*, Amsterdam, North-Holland, 1978.
[11] E. Sanchez-Palencia, *Non-Homogeneous Media and Vibration Theory,* Lecture Notes in Physics, Vol. 127, Springer-Verlag, Berlin, 1980.

[12] J.L. Lions, *Some Methode in the Mathematical Analysis of Systems and their Control*, Gordon and Breach, New York, 1981.
[13] O. van der Sluis, P.J.G. Schreurs, W.A.M. Brekelmans et al., Mech. Mater. 32 (2000) p.449.
[14] S. Mesarovic and J. Padbidri, Phil. Mag. 85 (2005) p.65.
[15] T.E. Lacy, D.L. McDowell and R. Talreja, Mech. Mater. 31 (1999) p.831.
[16] I.M. Gitman, H. Askes and L.J. Sluys, Eng. Fract. Mech. 74 (2007) p.2518.
[17] J.F.W. Bishop and R. Hill, Phil. Mag. 42 (1951) p.414.
[18] C. Miehe, J. Schroder and M. Becker, Comput. Methods Appl. Mech. Engrg. 191 (2002) p.4971.
[19] A.L. Gurson, J. Eng. Mater. T. ASME 99 (1977) p.2.
[20] P.H. Geubelle and J.S. Baylor, Compos. Part B Eng. 29B (1998) p.589.
[21] D.V. Kubair and P.H. Geubelle, Int. J. Solids Struct. 40 (2003) p.3853.
[22] K. Matouš, H.M. Inglis, X. Gu et al., Compos. Sci. Technol. 67 (2007) p.1694.
[23] G.M. Knott, T.L. Jackson and J. Buckmaster, AIAA J. 39 (2001) p.678.
[24] D. Rypl and Z. Bittnar, Engng Mech. 9 (2002) p.49.
[25] P.H. Geubelle, H.M. Inglis, J.D. Kramer et al. in *Proceedings of the Multiscale and Functionally Graded Materials Conference*, Hawaii, October 15–18, 2006.
[26] R.M. Christensen, J. Mech. Phys. Solids 38 (1990) p.379.

Downloaded By: [University of Illinois] At: 17:27 29 September 2008